AGU PUBLICATIONS

Geophysical Research Letters

RESEARCH LETTER
10.1002/2015GL065284

Key Points:
- Dispersed swell and infragravity wave-generated signals are observed 100 km from the shelf front
- Polarization analysis indicates infragravity band signal propagation characteristics from the front
- IG band signals propagate as Rayleigh-Lamb (flexural) waves in the ice shelf/water cavity system

Supporting Information:
- Supporting Information S1

Correspondence to:
P. D. Bromirski,
pbromirski@ucsd.edu

Citation:
Bromirski, P. D., A. Diez, P. Gerstoft, R. A. Stephen, T. Bolmer, D. A. Wiens, R. C. Aster, and A. Nyblade (2015), Ross ice shelf vibrations, *Geophys. Res. Lett.*, *42*, 7589–7597, doi:10.1002/2015GL065284.

Received 8 JUL 2015
Accepted 14 AUG 2015
Accepted article online 22 AUG 2015
Published online 16 SEP 2015

Ross ice shelf vibrations

P. D. Bromirski[1], A. Diez[1], P. Gerstoft[1], R. A. Stephen[2], T. Bolmer[2], D. A. Wiens[3], R. C. Aster[4], and A. Nyblade[5]

[1]Scripps Institution of Oceanography, University of California San Diego, La Jolla, California, USA, [2]Woods Hole Oceanographic Institution, Woods Hole, Massachusetts, USA, [3]Department of Earth and Planetary Sciences, Washington University in St. Louis, St. Louis, Missouri, USA, [4]Geosciences Department, Colorado State University, Fort Collins, Colorado, USA, [5]Department of Geosciences, Pennsylvania State University, University Park, Pennsylvania, USA

Abstract Broadband seismic stations were deployed across the Ross Ice Shelf (RIS) in November 2014 to study ocean gravity wave-induced vibrations. Initial data from three stations 100 km from the RIS front and within 10 km of each other show both dispersed infragravity (IG) wave and ocean swell-generated signals resulting from waves that originate in the North Pacific. Spectral levels from 0.001 to 10 Hz have the highest accelerations in the IG band (0.0025–0.03 Hz). Polarization analyses indicate complex frequency-dependent particle motions, with energy in several frequency bands having distinctly different propagation characteristics. The dominant IG band signals exhibit predominantly horizontal propagation from the north. Particle motion analyses indicate retrograde elliptical particle motions in the IG band, consistent with these signals propagating as Rayleigh-Lamb (flexural) waves in the ice shelf/water cavity system that are excited by ocean wave interactions nearer the shelf front.

1. Introduction

Buttressing ice shelves restrain ice drainage from the interior of Antarctica [*Rignot et al.*, 2002; *Joughin and Alley*, 2011]. Removal of this buttressing would trigger a speedup in ice flow into the ocean [*Scambos et al.*, 2004], causing sea level rise to accelerate. Thus, understanding ice shelf dynamics in response to climate change is important to anticipate acceleration of sea level rise. The catastrophic breakups of the Larsen B (2002) and Wilkins (2008) ice shelves along the Antarctic Peninsula [*Scambos et al.*, 2000, 2004] and measurement of significant thinning of the remaining West Antarctic ice shelves [*Paolo et al.*, 2015] indicate that this buttressing effect is decreasing and thus suggest that the Antarctic contribution to global sea level rise likely will increase over the next century.

The specific mechanisms initiating ice shelf collapse events remain only partially identified because the time scale of collapse is simply too short (hours to days) to allow sufficient satellite passes to adequately observe the process. Leading theories suggest that abundant free surface water (e.g., in ponds) fills preexisting crevasses, constituting the principle-enabling condition for collapse [*Scambos et al.*, 2009; *Banwell et al.*, 2013]. The mechanisms that produce the preexisting crevasses are unknown, although gravity wave impacts may contribute significantly [*Bromirski et al.*, 2010; *Sergienko*, 2010].

Changes in the Ross Sea climate (increasing storminess, changing wind and ocean circulation patterns, decreasing sea ice cover, and warming ocean) will significantly affect the Ross Ice Shelf (RIS) integrity and response. To identify changes in RIS response (that suggest weakening), it is important to establish present-day gravity wave-induced ice shelf response characteristics.

To investigate the response of the RIS to gravity wave forcing, a 34-station, spatially broad-scale, on-ice, broadband seismographic network (designated DRIS) was deployed during November 2014 (https://scripps.ucsd.edu/centers/iceshelfvibes/) (Figures 1a and 1b). The array was positioned to build on past observations [*MacAyeal et al.*, 2006] from a single shelf front station deployment in 2004–2006 (NIB, Figure 1a). Here we report on seismic data from three stations (DR09, DR10, and DR13) about 100 km from the RIS front (within 10 km of each other near DR10, Figure 1b) that were downloaded at the close of deployment operations at the end of November 2014, allowing for an initial assessment assessment of the RIS response to ocean forcing away from the shelf front during that month.

2. IG Wave and Swell-Generated Signals

Transformation of swell to infragravity (IG) waves is a nonlinear process that occurs in shallow water where $kh \ll 1$ [*Kinsman*, 1965], with k the wave number and h the water depth. Forced IG waves are generated in

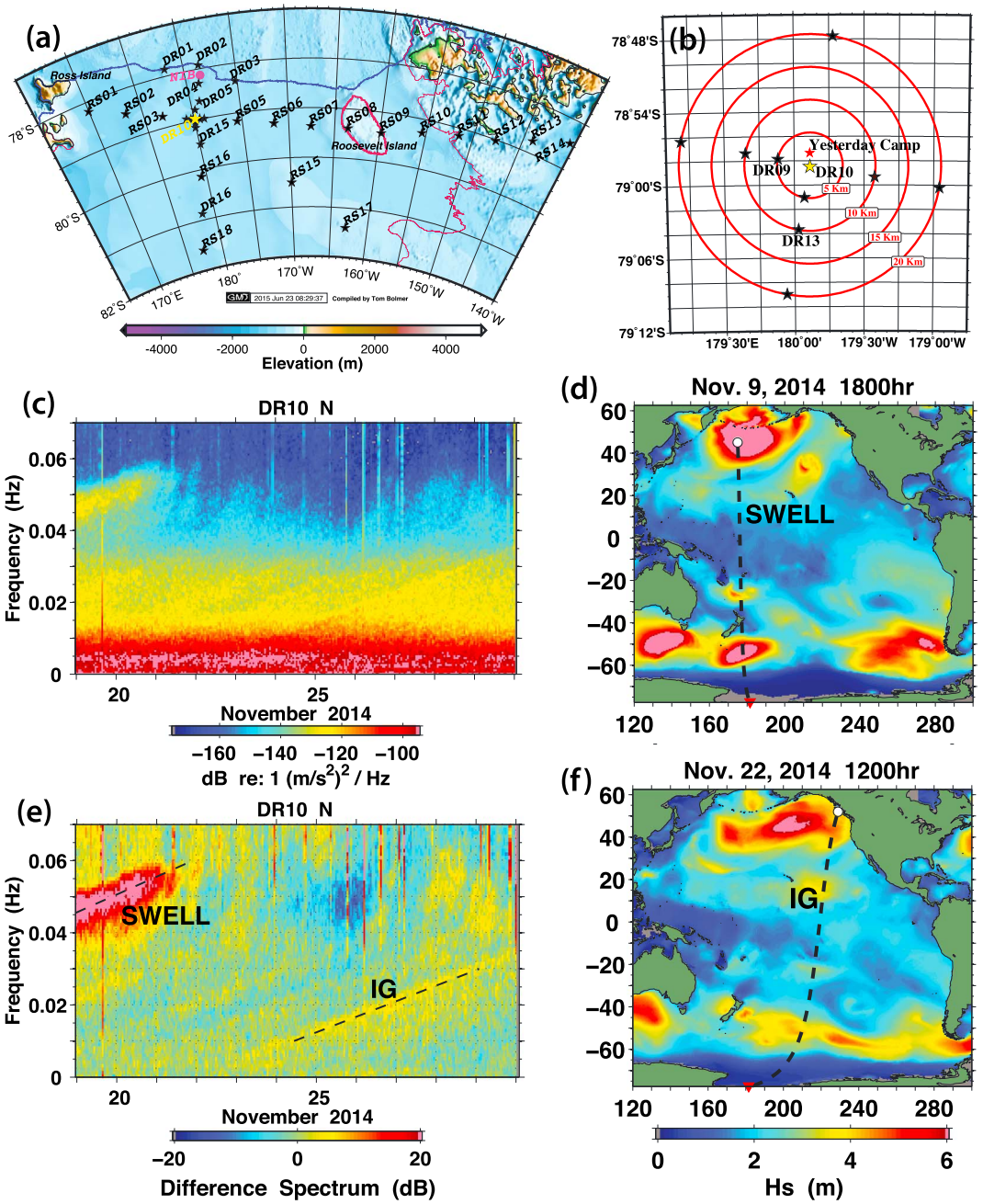

Figure 1. (a) Station locations on the Ross Ice Shelf, with the shelf front (blue line) indicated and estimated grounding-like location (magenta). Station NIB (red dot) was occupied during 2004–2006. (b) Locations of stations DR09 and DR13 near the DR10 location in Figure 1a. (c) Spectrogram displaying the temporal variability of spectral levels in the IG wave and swell frequency bands during 19–30 November 2014 for the north-south horizontal (N) component seismometer at DR10. (d) Snapshot of WAVEWATCH III (WW3) [*Tolman*, 2009] wave model significant wave height, Hs, distribution during a strong North Pacific storm event, and resulting swell propagation path to the RIS (dashed line) from an estimated generation location (white dot). (e) Difference spectra obtained by subtracting the median N component spectral levels. Note that this gives relative spectral level variability that should be compared only within the same frequency band. Dashed lines in Figure 1e indicate modeled swell and IG event arrivals, respectively, associated with wave events in Figures 1d and 1f. (f) Same as Figure 1d but showing the arrival of swell at the British Columbia coast (white dot) and resulting transformed IG wave path to the RIS (dashed line), giving the modeled IG arrival times in Figure 1e for the strongest IG band dispersed signal trend identified.

the surf zone by nonlinear subharmonic resonances [*Munk*, 1949; *Longuet-Higgins and Stewart*, 1962; *Herbers et al.*, 1994, 1995] and become refractively trapped along coastlines as a consequence of the sloping seafloor. Some of this energy leaks from the continental shelf and becomes free IG waves that can propagate transoceanically [*Bromirski et al.*, 2010].

In deep water, forced IG waves result from the nonlinear interaction of different phase velocity components of swell groups [*Battjes et al.*, 2004] and are considered "bound" waves since they travel with the swell group at the gravity wave deep-water approximation speed, resulting in bound IG and its carrier swell components arriving simultaneously. In contrast, free IG waves travel faster than swell in deep water and their speeds must be modeled with the gravity wave dispersion relation. As swell energy does not extend significantly below 0.03 Hz, extension (earlier arrival) of dispersed linear energy trends below 0.03 Hz indicates free IG energy.

The response of the RIS to forcing by ocean surface gravity waves depends on properties of the coupled ice shelf and sub-ice shelf water cavity system underlain by the solid Earth, as well as on the spatially variable internal structure, thickness, and elastic and viscoelatic properties of the ice. Flexing of ice shelves by long-period gravity waves, particularly IG waves, could provide additional externally generated stresses that can extend/expand existing fractures (rifts and/or crevasses) [*Goodman et al.*, 1980; *Wadhams*, 2000; *Squire*, 2007] and thus facilitate or trigger calving and perhaps collapse events.

Elastic waves and ice flexure are produced by gravity wave/ice shelf interactions, illustrated in Figure 2d, as well as tides. Because IG waves have much longer wavelengths than swell (e.g., about 16 km for 200 s IG waves and 1 km for 25 s swell in 700 m deep water at the RIS front), IG wave energy can flex the RIS across much greater distances. In addition, IG wave-induced vibrations may undergo resonant amplification when propagating through the ice shelf-subshelf cavity system (Figure 2d), with the resonance frequencies excited depending on ice shelf thickness [*Bromirski and Stephen*, 2012]. Modeling suggests that the amplitude of IG wave-induced flexural stresses decays away from the ice front at spatial scales varying from tens of kilometers for ocean swell to hundreds of kilometers for IG waves [*Sergienko*, 2010], consistent with gravimeter measurements [*Williams and Robinson*, 1979]. These fundamental phenomenological characteristics of the interaction of gravity wave energy with the ice shelf/cavity system are being investigated with the DRIS array, in particular, with the N-S linear transect (approximately orthogonal to the ice front) that extends from ice edge station DR02, near the former Nascent Iceberg seismograph site (NIB) [*MacAyeal et al.*, 2006; *Cathles et al.*, 2009], toward the grounding line to station RS18 (Figures 1a and 2d).

2.1. Seismic Observations

Seismic data were collected with three-component broadband seismometers (Nanometrics T120PHQ) buried about 1.5 m below the snow surface and connected by cable to digital recording (Quanterra Q330) and power systems placed in insulating boxes. Power is supplied by solar panels in austral summer and lithium batteries during winter, providing year-round continuous operation with Iridium state-of-health telemetry.

2.1.1. IG and Swell Spectral Amplitudes

Spectrograms from station DR10 (100 km from the shelf front) show time histories of swell and IG wave-induced signals (Figures 1c and 1e). Signal acceleration levels are strongest at the low end of the IG band (Figure 1c, $<$0.01 Hz), with IG band signals extending from 0.0025 to 0.033 Hz with rms displacement amplitudes of about 2 cm. The strongest long-period swell-induced signals (observed on 19–20 November) have amplitudes that are typically about 20 dB lower than IG band signals.

2.1.2. IG and Swell Source Locations

Gravity waves traveling in deep water are dispersed; i.e., their speed is inversely proportional to wave frequency. Dispersed swell and IG wave arrivals from specific source regions can be identified in spectrograms as bands of constant positive slope (Figure 1c). The slope of each slanting band is inversely proportional to the distance to the generation region. Signals generated by very long period swell (0.04–0.055 Hz) on 19–20 November and some of the IG wave-induced response (at frequencies $<$0.03 Hz) on 24–29 November are strongly dispersed (Figures 1c and 1e), indicating distant storm wave generation. These dispersed swell and IG signals can be more clearly identified in difference spectrograms from on-ice seismic station DR10, deployed prior to the other stations (Figure 1e). Transient vertical bands denote cultural noise or earthquake signals.

Remnants of Typhoon Nuri tracked across the Aleutian Islands into the Bering Sea during early November 2014 [*LeComte*, 2015]. Waves generated by winds from this storm were hindcast using WAVEWATCH III [*Tolman*, 2009], as forced by National Centers for Environmental Prediction-National Center for Atmospheric Research

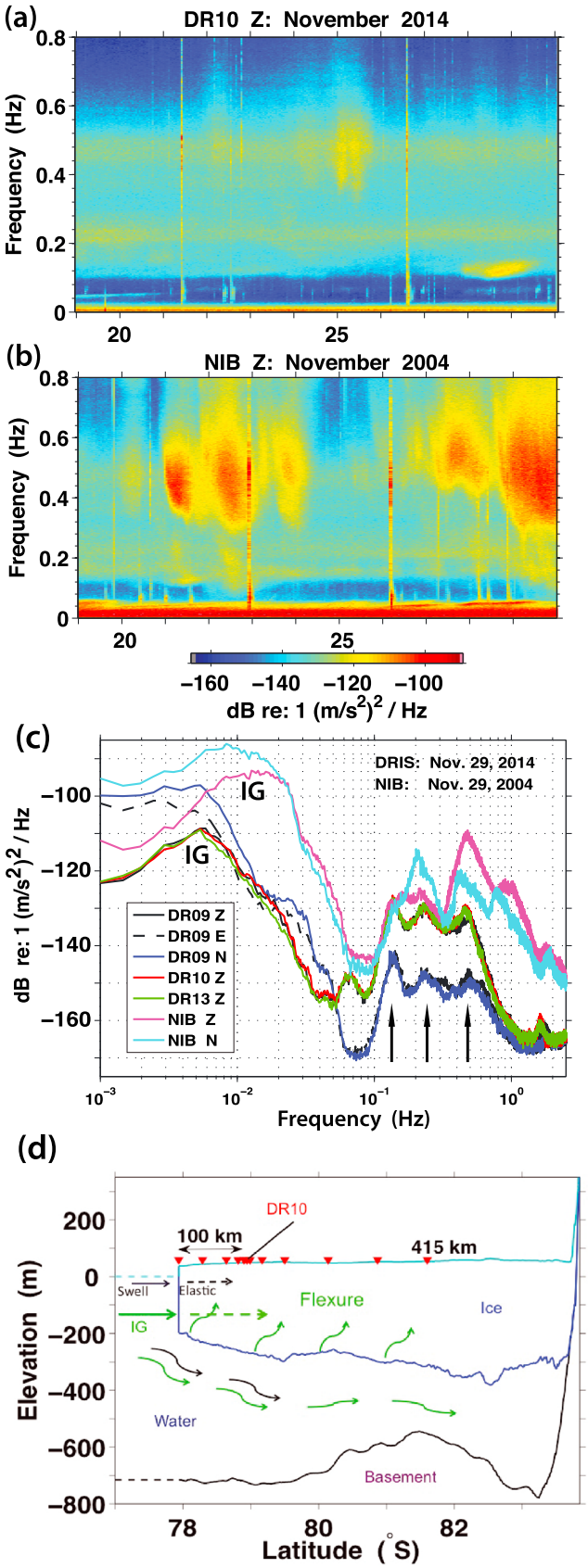

reanalysis winds [*Kalnay et al.*, 1996]. Continuous 3 h wave model significant wave height, Hs, hindcasts for all of November 2014 allow estimation of probable distant wave generation times and locations. The distribution of high-amplitude waves from Typhoon Nuri during 9 November is shown in Figure 1d. The trailing southwest quadrant of North Pacific cyclonic storm systems produce waves directed toward the RIS [*Bromirski et al.*, 2010]. Modeling of the propagation of swell from the estimated time and location of generation (Figure 1d, white dot) using the gravity wave dispersion relation along a great circle path to the RIS gives wave arrival times (dashed line 19–20 November, Figure 1e) that closely match the observed positive-anomaly signals at DR10. The source time and location would be better constrained if data prior to 19 November were available.

When swell from another storm later in November reached the British Columbia coast (Figure 1f), shallow-water-transformed swell produced free IG waves that propagated along a great circle path to the RIS and excited the dispersed IG band signals in Figure 1e. Inverting the IG-forced signal dispersion trend for this event, using the gravity wave dispersion relation gives a source distance of about 12,000 km consistent with the presumed generation location and modeled dispersion trend. Other lower energy dispersion trends having

Figure 2. (a) Power spectral density variation at DR10 for the vertical (Z) acceleration response during 19–29 November 2014, showing two relatively strong, continuous bands centered near 0.24 and 0.48 Hz. (b) Same as Figure 2a except for ice front station NIB during November 2004. (c) Median acceleration power spectral densities at seismic stations DR09, DR10, and DR13 on 29 November 2014 and shelf front station NIB on 29 November 2004. Peaks near 0.13, 0. 24, and 0.48 are identified with arrows. (d) BEDMAP2 *Fretwell et al.* [2013] cross section of ice/water geometry along a transect near stations roughly orthogonal to the RIS front (see Figure 1a). Also shown are schematic representations of possible excitation locations.

similar slopes are identifiable in Figures 1c and 1e, suggesting that the northeastern Gulf of Alaska and British Columbia coasts are common source areas for free IG waves impacting the RIS.

Note that the presumed wave generation locations for both swell and IG (white circles in Figures 1d and 1f) are not unique, as any location along an arc that satisfies the source distance at the origin time will produce the dispersion trends observed. Locations of wave activity identified in an animation of the wave model hindcast constrain likely source locations.

Because the wave model hindcast shows high-amplitude waves north of the RIS between 50°S and 60°S (Figure 1d and 1f), we contend that the general lack of swell-induced energy in the [0.06, 0.09 Hz] band (Figure 2a) is in part a consequence of damping of swell by sea ice [*Wadhams et al*., 1988]. Longer-period gravity waves, especially IG, are less affected by sea ice damping [*Wadhams and Doble*, 2009; *Bromirski and Stephen*, 2012] and thus IG wave-generated signal levels will be less affected.

A significant portion of the IG wave energy < 0.01 Hz does not exhibit dispersion (Figures 1c). Because the water depth at the RIS front (~700 m) is too deep for local shallow-water forced-IG generation [*Longuet-Higgins and Stewart*, 1962; *Herbers et al*., 1994, 1995], regional swell group bound IG waves must provide a significant portion of the forcing of the nondispersed RIS response in the IG band. However, the higher amplitude signals in Figure 1e are associated with free IG waves, suggesting that shoaling at the continental shelf boundary and/or refraction focusing while traversing the continental shelf may significantly amplify IG wave forcing of the RIS. Other lower amplitude energy bands are observed having dispersion trend slopes similar to the IG signals identified, suggesting that IG wave arrivals from the North Pacific are common, consistent with modeled strong IG wave generation along the coasts of the northeast Pacific [*Ardhuin et al*., 2014].

3. Signal Propagation Characteristics From Polarization Analysis

3.1. Spectral Levels

Spectrograms of vertical component acceleration time histories at DR10 and NIB are shown in Figures 2a and 2b. Spectral levels at NIB are generally much higher, potentially due to stronger gravity wave forcing, edge effects associated with proximity to the shelf front, and/or an accentuated response due to the different geometry and characteristics of the ice/water system (Figure 2d; note thinner ice and deeper water at NIB). Persistent spectral bands occur near 0.24 and 0.48 Hz at DR10 and NIB, although the 0.48 Hz resonance band at NIB is commonly obscured by episodic higher spectral levels between 0.3 and 0.7 Hz, previously attributed to periods when stronger ocean forcing occurs that amplifies this resonance [*Bromirski and Stephen*, 2012].

Median acceleration power spectral densities at stations DR09, DR10, and DR13 (November 2014) show spectral peaks between 0.001 and 1 Hz (Figure 2c) for the vertical (Z), north (N), and east (E) components. Also shown in Figure 2c are spectral levels of N and Z components at ice front station NIB (November 2004). Median vertical spectral levels at DR09, DR10, and DR13 (Figure 2c) are within a few decibels of each other and often overlap. North-south (N) IG spectral levels (0.0025–0.01 Hz) are higher than vertical levels at both the NIB and DRIS stations (compare Z with N in Figure 2c).

The dominant vertical spectral peak at DR09 occurs in the IG wave band near 0.006 Hz and at NIB between 0.01 and 0.02 Hz. The higher IG band peak amplitudes indicate that the longer wavelength IG waves elicit a stronger response of the RIS than swell.

3.2. Polarization Analysis

Propagation characteristics, wave type, and potential source areas of the wave-induced signals can be deduced from polarization analysis [*Jurkevics*, 1988; *Vidale*, 1986]. The eigenvalues and eigenvectors are obtained for the spectral density matrix of the three-component seismic data, corrected for the seismometer response, from an average of three consecutive 1 h data segments. The eigenvector (normalized and rotated to maximize the length of its real part) belonging to the largest eigenvalue is used to calculate the back azimuth, the sagittal angle, and the ellipticity of the polarization.

The back azimuth and sagittal angle are calculated using tangent functions of the real part of the three elements of this eigenvector associated with the Z, N, and E displacement components [*Jurkevics*, 1988]. We assume that the dominant signal excitation is forced by swell and IG waves arriving at the RIS front to the north. Thus, northerly azimuths were chosen when north-south motions were identified. The

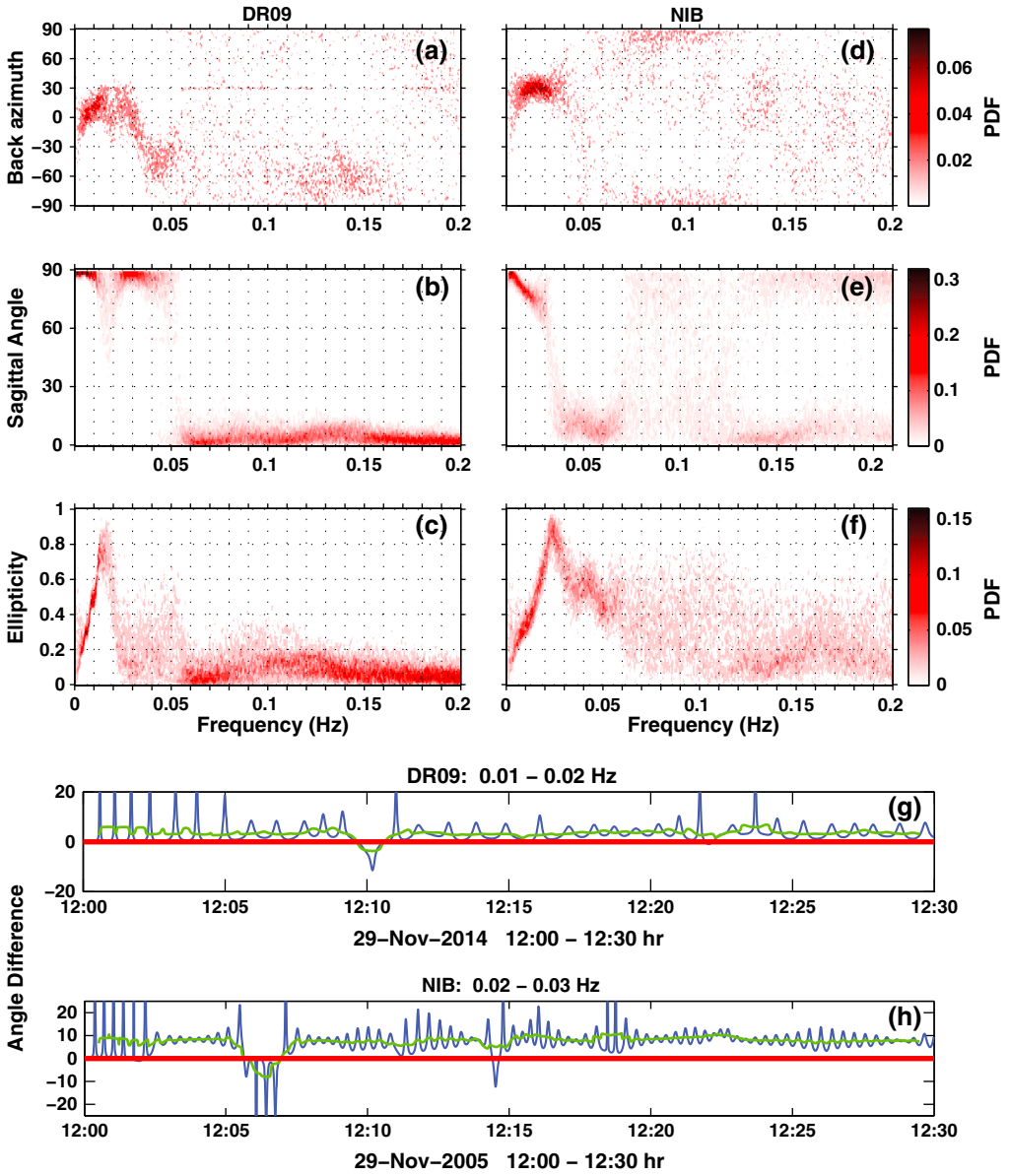

Figure 3. (a)–(c) Probability density functions (PDF) of polarization attributes comparing aspects of particle motions from seismometer data collected (a)–(c) at station DR09 during November 2014 and (d)–(f) at NIB during November 2004, both records spanning approximately 11 days. (Figures 3a and 3d) Back azimuth, degrees from north (positive = east); (Figures 3b and 3e) sagittal angle, degrees from vertical (0° = vertical and 90° = horizontal particle motion, respectively); and (Figures 3c and 3f) ellipticity, 0 = linear particle motion, 1 = circular motion. (g) Representative angle difference in degrees between the vertical and horizontal motions for successive time steps during a 30 min period at DR09 on 29 November 2014 for band-pass-filtered 1 samples per second data spanning the 0.01–0.02 Hz frequency band, with 1 min averages (green curves) overlaid to identify dominant motions. Positive angle differences indicate retrograde particle motions. (h) Same as Figure 3g except for NIB over 0.02–0.03 Hz.

ellipticityis determined from the ratio of the imaginary part of the normalized eigenvector to the real part [*Vidale*, 1986]. Linear polarization corresponds to an ellipticity value of zero, whereas ellipticity of one indicates circular particle motion. The horizontal component of particle motion, with assumption of wave type, enables resolution of the back azimuth. When the particle motion is vertical, azimuthal estimates are not reliable.

This methodology gives the variability of the three polarization attributes versus time and frequency (see Figure S1 in the supporting information). To examine their dominant tendencies as a function of frequency, empirical probability density functions (PDF) were formed from the polarization attribute time-frequency histories. The PDF distributions for station DR09 (Figures 3a–3c) during 20–30 November 2014 and ice front

station NIB (Figures 3d–3f) during November 2005 compare signal characteristics between the shelf front (NIB) and intrashelf (DR09) locations (see Figure S2in the supporting information for an expanded frequency range, 0–0.7 Hz).

3.2.1. Dominant Polarization Characteristics

In the IG band below 0.03 Hz, both the DR09 and NIB stations show back azimuths from the north (Figures 3a and 3d, respectively) generally clustering around 0° and 30°, respectively, suggesting that this energy results from IG wave forcing at the shelf front. This is associated with elliptical polarization, giving a sagittal angle of near 90° at DR09, consistent with horizontally propagating flexural waves. For station DR09, these sagittal angles and back azimuths extend up to about 0.05 Hz, compared with about 0.025 Hz at NIB. The 0.03–0.05 Hz band includes both swell- and IG-wave-induced signals. In contrast to DR09, particle motion at NIB is nearly vertical with a stronger elliptical component in the 0.03–0.5 Hz band, but with no clear back azimuth tendency.

Above 0.05 Hz at DR09, the dominant particle motion is vertical (sagittal angle 0°), with generally linear polarized waves dominating, although there is some indication of elliptical motion near 0.1 Hz at DR09 (Figure 3c). The predominantly rectilinear, vertical particle motions above 0.05 Hz are consistent with vertically polarized transverse waves propagating horizontally.

The variability of polarization attributes at shelf front station NIB between 0.05 and 0.35 Hz (Figure S2) differs from DR09, with apparently more complex motions that include both vertical and horizontal sagittal angles and a greater tendency for elliptical motions. These more elliptical nonvertical motions allow some azimuthal resolution, suggesting signals originating from the east and west as well as from the north.

At frequencies above 0.5 Hz (Figure S2), all polarization attributes show increasingly strong scattering at DR09, although the tendency for vertical particle motion persists. Similar to DR09, NIB data also generally show vertical and linear polarization between 0.35 and 0.7 Hz (Figure S2).

3.2.2. Prograde Versus Retrograde Elliptical Particle Motion

Swell and IG waves have prograde circular and elliptical particle motions. Some energy from this gravity wave motion may transfer these motions to the ice [*Wadhams and Doble*, 2009]. In contrast, asymmetric Rayleigh-Lamb (flexural) and crustal Rayleigh waves have retrograde elliptical motions [*Lamb*, 1917].

Prograde motions can be differentiated from retrograde motions for assumed edge-normal, poleward propagating seismic signals by examining continuous phase differences between vertical and north-south component displacements. Consecutive angle differences were obtained at successive time steps from Z and N band-pass-filtered displacements for frequency bands that contained the peaks in ellipticity at DR09 and NIB (Figures 3c and 3f, respectively). Figures 3g and 3h show that a positive angle difference persists at these frequencies (and for similar analyses across the entire IG band < 0.03 Hz, not shown), indicating retrograde motions.

3.2.3. Correspondence of Relative Spectral Levels and Polarization Analysis

The observed frequency variations of the polarization attributes for both the DR09 and NIB stations (Figure 3) correspond reasonably well to relative spectral level variations and differences between vertical (Z), north-south (N), and east-west (E) components shown in Figure 2c. Below 0.05 Hz at DR09 where generally $N > Z$, back azimuth angles can be reasonably well resolved as from a northerly direction with horizontal sagittal angles (Figures 2a and 2b). In contrast, above 0.05 Hz where generally $Z > N$, sagittal angles are vertical and the back azimuth cannot be resolved. Similar behavior is observed at ice front station NIB, but with the transition from dominant horizontal to dominant vertical motion occurring at a lower frequency (at about 0.025 Hz; Figure 3e), where N levels approach Z levels (Figure 2c).

Consistent linear polarization with vertical particle motion is observed in a relatively wide frequency band at DR09 (0.15–0.55 Hz) that includes the apparent RIS resonance peak near 0.48 Hz (Figures S2a–S2c in the supporting information), corresponding well with the relative spectral level variation at DR09 in this band where Z levels are consistently about 25 dB higher than N levels. Similarly at NIB, linear polarization and vertical particle motion are dominant near the 0.48 Hz peak (Figures S2e and S2f).

4. Discussion

Long-period swell and IG waves have much longer wavelengths than the shelf thickness, suggesting that wave energy within the water cavity near the front might couple prograde gravity-wave motions into similar

shelf motions. However, retrograde elliptical motions propagating from the north (shelf front) dominate the IG band at DR09 (Figures 3g and 3h). IG band amplitudes at NIB are more than 5 orders of magnitude (more than 50 dB) greater than at Scott Base, Antarctica [*Bromirski and Stephen*, 2012]. Because crustal Raleigh waves would attenuate much less over distances on the order of the 300 km separating the RIS stations, this indicates that the IG band signals observed at DR09 and NIB are not Rayleigh waves. Rayleigh-Lamb waves are excited in thin "plates" (or ice shelves) where the wavelength of the forcing function is much greater than the plate thickness, criteria met by IG wavelengths (~15 km) compared with the RIS thickness (~300 m). Hence, retrograde motions at both DR09 and NIB combined with northerly back azimuths (Figures 3a and 3d) and amplitude and wavelength considerations indicate that the IG band signals at DR09 are consistent with Rayleigh-Lamb flexural waves excited nearer the shelf front that propagate within the ice shelf/water cavity system.

Because most swell energy is concentrated near the ocean surface, swell impacts at the 200 m thick shelf front are expected to produce primarily elastic wave energy, consistent with the vertical sagittal angles and linear ellipticity observed at DR09 in the swell band and at higher frequencies (Figures 3b, 3c, S2b, and S2c). Frequency bands where vertical levels are much higher than horizontal (Figure 2c, $Z > N$) and vertical particle motion and linear polarization dominate, e.g., at DR09 between 0.15 and 0.6 Hz (Figure S2), may result from locally generated elastic wave energy produced by flexing of the RIS.

Remotely generated double-frequency microseism Rayleigh waves [*Bromirski and Duennebier*, 2002] are the probable source of the signals observed in the 0.1–0.15 Hz band on 28–29 November (Figure 2a), represented by the 0.13 Hz peak in Figure 2c. Polarization analysis back azimuth estimates (Figure S1) indicate that these signals arrive from the southeast quadrant, suggesting their generation along the Antarctic Peninsula coast. Because there is relatively little swell energy above 0.1 Hz [*Bromirski et al*., 1999], the spectral peaks near 0.24 and 0.48 Hz must result from properties and geometry of the ice shelf/water cavity system. A peak near 0.48 Hz is also observed at NIB (Figure 2b, magenta curve), suggesting that this peak may represent an eigenfrequency of the RIS [*Bromirski and Stephen*, 2012] that is dependent on the ice and water layer thicknesses.

5. Conclusions

Gravity-wave-induced vibrations are clearly observed 100 km from the shelf front, with IG wave band induced signals dominating the spectrum, indicating that IG-wave-induced Rayleigh-Lamb flexural wave energy penetrates well into the interior of the Ross Ice Shelf toward the grounding zone. Differences in spectral variations between the intrashelf DR09 and shelf front NIB stations and in the polarization analysis are possibly the result of differences in (1) the thicknesses and structure of the ice shelf/water system, (2) storm activity variations resulting in differences in swell and IG wave energy levels, (3) proximity to the RIS front, i.e., conversion of near-field excitation to other far-field wave types, and/or (4) sea ice extent and concentration.

Further observations being collected by the RIS broadband seismometer array over the next 2 years will better characterize the amplitude and spatiotemporal variability of the RIS response to swell and IG waves. Understanding of the RIS response to ocean wave impacts will improve glaciological understanding and modeling of ocean wave interactions with ice shelves and their influence on shelf integrity.

Acknowledgments

Bromirski, Diez, and Gerstoft were supported by NSF grant PLR 1246151. Stephen and Bolmer were supported by NSF grant PLR-1246416. Wiens, Aster, and Nyblade were supported under NSF grants PLR-1142518, 1141916, and 1142126, respectively. Bromirski also received support from the California Department of Parks and Recreation, Division of Boating and Waterways under contract 11-106-107. The NIB data were collected under NSF grant OPP-0229546 and were downloaded from the IRIS DMC archives. Seismic instruments and on-ice installation support were provided by the Incorporated Research Institutions for Seismology (IRIS) through the PASSCAL Instrument Center at New Mexico Tech. Data collected will be available through the IRIS Data Management Center. The facilities of the IRIS Consortium are supported by the National Science Foundation under cooperative agreement EAR-1261681 and the DOE National Nuclear Security Administration. Wave model data were obtained from F. Ardhuin, IFREMER. We thank Patrick Shore, Cai Chen, Rob Anthony, and Reinhard Flick for their help with field operations. Logistical support from the U.S. Antarctica Program in McMurdo is much appreciated.

The Editor thanks two anonymous reviewers for their assistance in evaluating this paper.

References

Ardhuin, F., A. Rawat, and J. Aucan (2014), A numerical model for free infragravity waves: Definition and validation at regional and global scales, *Ocean Modeling*, *77*, 20–32.

Banwell, A. F., D. R. MacAyeal, and O. V. Sergienko (2013), Break-up of the Larsen B Ice Shelf triggered by chain-reaction drainage of supraglacial lakes, *Geophys. Res. Lett.*, *40*, 5872–5876, doi:10.1002/2013GL057694.

Battjes, J. A., H. J. Bakkenes, T. T. Janssen, and A. R. van Dongeren (2004), Shoaling of subharmonic gravity waves, *J. Geophys. Res.*, *109*, C02009, doi:10.1029/2003JC00183.

Bromirski, P. D., and F. K. Duennebier (2002), The near-coastal microseism spectrum: Spatial and temporal wave climate relationships, *J. Geophys. Res.*, *107*(B8), 2166, doi:10.1029/2001JB000265.

Bromirski, P. D., and R. A. Stephen (2012), Response of the Ross Ice Shelf, Antarctica, to ocean gravity-wave forcing, *Ann. Glaciol.*, *53*(60), doi:10.3189/2012AoG60A058.

Bromirski, P. D., R. E. Flick, and N. Graham (1999), Ocean wave height determined from inland seismometer data: Implications for investigating wave climate changes in the NE Pacific, *J. Geophys. Res.*, *104*(C20), 20,753–20,766, doi:10.1029/1999JC900156.

Bromirski, P. D., O. V. Sergienko, D. R. MacAyeal (2010), Transoceanic infragravity waves impacting Antarctic ice shelves, *Geophys. Res. Lett.*, *37*, L02502, doi:10.1029/2009GL041488,

Cathles, L. M., IV, E. A. Okal, and D. R. MacAyeal (2009), Seismic observations of sea swell on the floating Ross Ice Shelf, Antarctica, *J. Geophys. Res.*, *114*, F02015, doi:10.1029/2007JF000934.

Fretwell, P., et al. (2013), Bedmap2: Improved ice bed, surface and thickness datasets for Antarctica, *Cryosphere*, *7*, 375–393, doi:10.5194/tc-7-375-2013.
Goodman, D. J., P. Wadhams, and V. A. Squire (1980), The flexutal response of a tabular ice island to ocean swell, *Ann. Glaciol.*, *1*, 23–27.
Herbers, T. H. C., S. Elgar, and R. T. Guza (1994), Infragravity-frequency (0.005–0.05 Hz) motions on the shelf. Part I: Forced waves, *J. Phys. Oceanogr.*, *24*(5), 917–927.
Herbers, T. H. C., S. Elgar, and R. T. Guza (1995), Generation and propagation of infragravity waves, *J. Geophys. Res.*, *100*(C12), 24,863–24,872, doi:10.1029/95JC02680.
Joughin, I., and R. B. Alley (2011), Stability of the West Antarctic ice sheet in a warming world, *Nat. Geosci.*, *4*, doi:10.1038/NGEO1194.
Jurkevics, A. (1988), Polarization analysis of three-component array data, *Bull. Seismol. Soc. Am.*, *78*(5), 1725–1743.
Kalnay, E., et al. (1996), The NCEP/NCAR 40-year reanalysis project, *Bull. Am. Meteorol. Soc.*, *77*, 437–471.
Kinsman, B. (1965), *Wind Waves: Their Generation and Propagation on the Ocean Surface*, 676 pp., Prentice-Hall Inc., Englewood Cliffs, N. J.
Lamb, H. (1917), On waves in an elastic plate, *Proc. R. Soc. London, Ser. A*, *93*, 114–128.
LeComte, D. (2015), International weather highlights 2014: Winter storms, typhoons, hurricanes, and flooding, *Weatherwise*, *68*(3), 20–26.
Longuet-Higgins, M., and R. W. Stewart (1962), Radiation stress and mass transport in gravity waves, with application to "surf beats", *J. Fluid Mech.*, *13*(4), 481–504.
MacAyeal, D. R., et al. (2006), Transoceanic wave propagation links iceberg calving margins of Antarctica with storms in tropics and Northern Hemisphere, *Geophys. Res. Lett.*, *33*, L17502, doi:10.1029/2006GL027235.
Munk, W. H. (1949), Surf beats, *Trans. AGU*, *30*(6), 849–854.
Paolo, F. S., H. A. Fricker, and L. Padman (2015), Volume loss from Antarctic ice shelves is accelerating, *Sci. Express*, doi:10.1126/science.aaa0940.
Rignot, E. J., D. G. Vaughan, M. Schmeltz, T. Dupont, and D. MacAyeal (2002), Acceleration of Pine Island and Thwaites Glaciers, West Antarctica, *Ann. Glaciol.*, *34*, 189–194.
Scambos, T., C. Hulbe, M. Fahnestock, and J. Bohlander (2000), The link between climate warming and ice shelf break-ups in the Antarctic Peninsula, *J. Glaciol.*, *46*(154), 516–530.
Scambos, T., H. A. Fricker, C.-C. Liu, J. Bohlander, J. Fastook, A. Sargent, R. Massom, and A.-M. Wu (2009), Ice shelf disintegration by plate bending and hydro-fracture: Satellite observations and model results of the 2008 Wilkins ice shelf break-ups, *Earth Planet. Sci. Lett.*, *280*(1–4), 51–60.
Scambos, T. A., J. A. Bohlander, C. A. Shuman, and P. Skvarca (2004), Glacier acceleration and thinning after ice shelf collapse in the Larsen B embayment, Antarctica, *Geophys. Res. Lett.*, *31*, L18402, doi:10.1029/2004GL020670.
Sergienko, O. V. (2010), Elastic response of floating glacier ice to impact of long-period ocean waves, *J. Geophys. Res.*, *115*, F04028, doi:10.1029/2010JF001721.
Squire, V. (2007), Of ocean waves and sea-ice revisited, *Cold Reg. Sci. Technol.*, *49*(2), 110–133.
Tolman, H. L. (2009), User manual and system documentation of WAVEWATCH III, version 3.14, Technical Note, U.S. Dep. of Commerce, NOAA, NWS, NCEP, Ocean Modeling Branch Contribution, 5200 Auth Road, Camp Springs, Md.
Vidale, J. E. (1986), Complex polarization analysis of particle motion, *Bull. Seismol. Soc. Am.*, *76*(5), 1393–1405.
Wadhams, P. (2000), *Ice in the Ocean*, 368 pp., Taylor and Francis, London.
Wadhams, P., and M. J. Doble (2009), Sea ice thickness measurement using episodic infragravity waves from distant storms, *Cold Reg. Sci. Technol.*, *56*, 98–101.
Wadhams, P., V. A. Squire, D. J. Goodman, A. M. Cowan, and S. C. Moore (1988), The attenuation rates of ocean waves in the marginal ice zone, *J. Geophys. Res.*, *93*(C6), 6799–6818, doi:10.1029/JC093iC06p06799.
Williams, R. T., and E. S. Robinson (1979), Ocean tide and waves beneath the Ross Ice Shelf, Antarctica, *Science*, *203*, 443–445.